Electrically-driven oxygen vacancy aggregation and displacement in $YBa_2Cu_3O_{7-\delta}$ films

Simon Collienne Stefan Marinković Alejandro Fernández-Rodríguez Narcís Mestres Anna Palau Alejandro V. Silhanek**

S. Collienne, S. Marinković, A. V. Silhanek
Experimental Physics of Nanostructured Materials, Q-MAT, CESAM, Université de Liège, B-4000 Sart Tilman, Belgium
Email Address: scollienne@uliege.be, asilhanek@uliege.be
A. Fernández-Rodríguez, N. Mestres, A. Palau
Institut de Ciència de Materials de Barcelona, ICMAB-CSIC, Campus UAB, 08193 Bellaterra, Spain

Keywords: *YBCO, electromigration, oxygen motion*

Combining direct visualization of current-induced oxygen migration through optical microscopy and finite element modeling of driven oxygen diffusion, we are able to estimate the average activation energy of oxygen motion in the crystallographic *ab*-plane of *c*-axis oriented polycrystalline $YBa_2Cu_3O_{7-\delta}$ films. Experiments and modeling are compared side-by-side for the case of constant current electromigration as well as for a train of current pulses of varying amplitude. The simulations reproduce the induced resistance changes after electromigration and confirm a high degree of spatial inhomogeneity in the stoichiometry. Assuming a temperature and oxygen concentration dependent resistivity, we are able to capture the change of superconducting critical temperature, normal state resistance, and the development of multistep transitions as a function of the electromigration history. The simulations are further applied to scrutinize the influence of activation energy, disorder in oxygen content and initial oxygen concentration on the electromigration process. These results shed new light on the non-local modifications produced by the electromigration process on oxide conductors.

1 Introduction

The copper oxide $YBa_2Cu_3O_{7-\delta}$ (YBCO) is arguably one of the most widely investigated materials in the last decades due in part to its rich variety of electronic phases spanning from antiferromagnetic semiconducting, non-Fermi liquid to superconducting behavior.[1] The key ingredients allowing to navigate through these phases are oxygen stoichiometry and oxygen ordering. This sensitivity to oxygen content is not exclusive to this material but seems to be generally observed in a vast majority of complex oxide compounds. From a technological standpoint, it is imperative to understand and master oxygen diffusion through thermal processing, in order to achieve high-end coated-conductors and reliable bipolar non-volatile resistive switchers. Consequently, an understanding of the chemical diffusion in YBCO may bear profound implications to a large diversity of oxides materials and their derived applications.
The variation of oxygen concentration in YBCO mostly occurs in the O(1) sites of the CuO chains along the crystallographic *b*-axis. In the superconducting orthorhombic phase ($\delta \approx 0$), if the O(1) atom migrates to a neighboring vacant O(5) site, it will find a channel along the *b*-axis direction with essentially no diffusion barrier.[2] It is expected that the associated activation energy E_a will depend strongly on the amount of oxygen atoms per unit cell, with E_a lowering as the number of available sites (i.e. δ) increases. This has been indeed experimentally confirmed in YBCO crystals for which it was reported $E_a = 1.3$ eV for $\delta = 0$ and $E_a = 0.5$ eV for $\delta = 0.38$.[3] Concomitant isotopic ^{18}O tracer diffusion measurements by Rothman *et al.*[4] indicated a value of $E_a = 0.97$ eV in the *ab*-plane of bulk YBCO pellets. Similar value was reported for YBCO single crystals with stoichiometry $\delta = 0.5$ by Veal *et al.*[5] through thermal annealing process. Soon after, Choi *et al.*[6] calculated the oxygen tracer diffusion coefficients using the cluster variation method in conjunction with the path probability method for a perfect lattice and showed that activation energies are significantly dependent on the oxygen density and the degree of long-range order, with $E_a = 0.8$ eV in the tetragonal phase and $E_a = 1.2$ eV in the orthorhombic phase. The fact that the activation energies for the oxygen diffusion decrease with decreasing oxygen content was also confirmed in laser ablated thin films by Krauns and Krebs.[7] In ref.[8] a migration energy as

low as 0.3 eV has been calculated for oxygen ions in the *ab*-plane using a shell model for the orthorhombic phase. A more in-depth investigation of oxygen tracer diffusion in untwinned single-crystalline YBCO showed that the diffusion along the *b* direction can be at least 100 times faster than diffusion along the *a* direction.[9] In all cases, diffusion along *c* axis was reported to be substantially slower than within the *ab* plane.

The dispersion observed in the reported values of the activation energy can be partially accounted for by the fact that a distribution of activation energies depending on the local environment is to be expected.[10] More importantly, several paths of oxygen diffusion may coexist with diffusion along the surface, the grain boundaries, and twin boundaries dominating over lattice diffusion as demonstrated by comparing single crystals to polycristalline YBCO.[11] This has been recently demonstrated via molecular dynamics simulations by Wang *et al.*[12] where it was shown that oxygen diffusion in YBCO can be enhanced in grain boundaries with an activation energy exponentially decreasing with the grain boundary angle.

In general, the experimental investigations presented above rely on diffusive processes induced by thermal annealing under controlled environmental conditions. Recently, a radically different approach consisting in current-induced migration of oxygen, has been proposed.[13] This technique has been implemented to scan the entire temperature-hole concentration phase diagram in a single and the same sample.[14] In this case, the agglomeration of oxygen vacancies manifests itself as a zone of higher reflectivity thus permitting to track the temporal evolution of the affected area by optical microscopy.

In this work, we provide optical microscopy inspection of oxygen vacancy migration stimulated by high current densities and complement this study with finite elements modeling in order to quantitatively assess the effect of effective activation energy for oxygen diffusion. We demonstrate that the oxygen disorder induced by electromigration can take place simultaneously in several spots along the transport bridge. Low frequency AC electromigration evidences an irreversible process which is accentuated if a concentration-dependent activation energy is introduced. The modeling is able to capture the evolution of the superconducting transition after electromigration as well as the oxygen vacancy mapping.

2 Results and Discussion

The investigated superconducting samples are YBCO thin films patterned into a multiterminal bridge shape as shown in Figure 1. Eight voltage probes are used to individually assess the electrical response of the three bridges connected in series. The length × width of the two side bridges is 5 μm × 3 μm, whereas for the inner bridge the dimensions are 3 μm × 1 μm. All films exhibited superconducting critical temperatures $T_c \sim 85$ K consistent with $\delta \sim 0.2 \pm 0.05$ defined as the maximum slope of the resistance vs temperature $R(T)$ curve.

2.1 Optical and electrical probing of oxygen vacancies migration

The electromigration process was achieved through two different approaches, namely (i) constant current measurements and (ii) amplitude-dependent current pulses.

2.1.1 DC electric stress

For the constant current measurements, a DC current is maintained by the source and the resistance R of each of the three bridges is independently monitored as a function of the time elapsed t. The inset in the left panel of Figure 2 shows a scheme of the current polarity imposed and the color code used to indicate the response of each bridge. At 3 mA (corresponding to 3 MA cm^{-2} in the central bridge), a small increase of the resistance as a function of time is observed in the three bridges. When the current is increased to 6 mA the initial resistance increases substantially due to Joule heating. Surprisingly, while the left and right side bridges exhibit an increase of resistance with time, the central bridge shows a progressive decrease. Further increasing the current to 8 mA, shows that all three bridges reached a

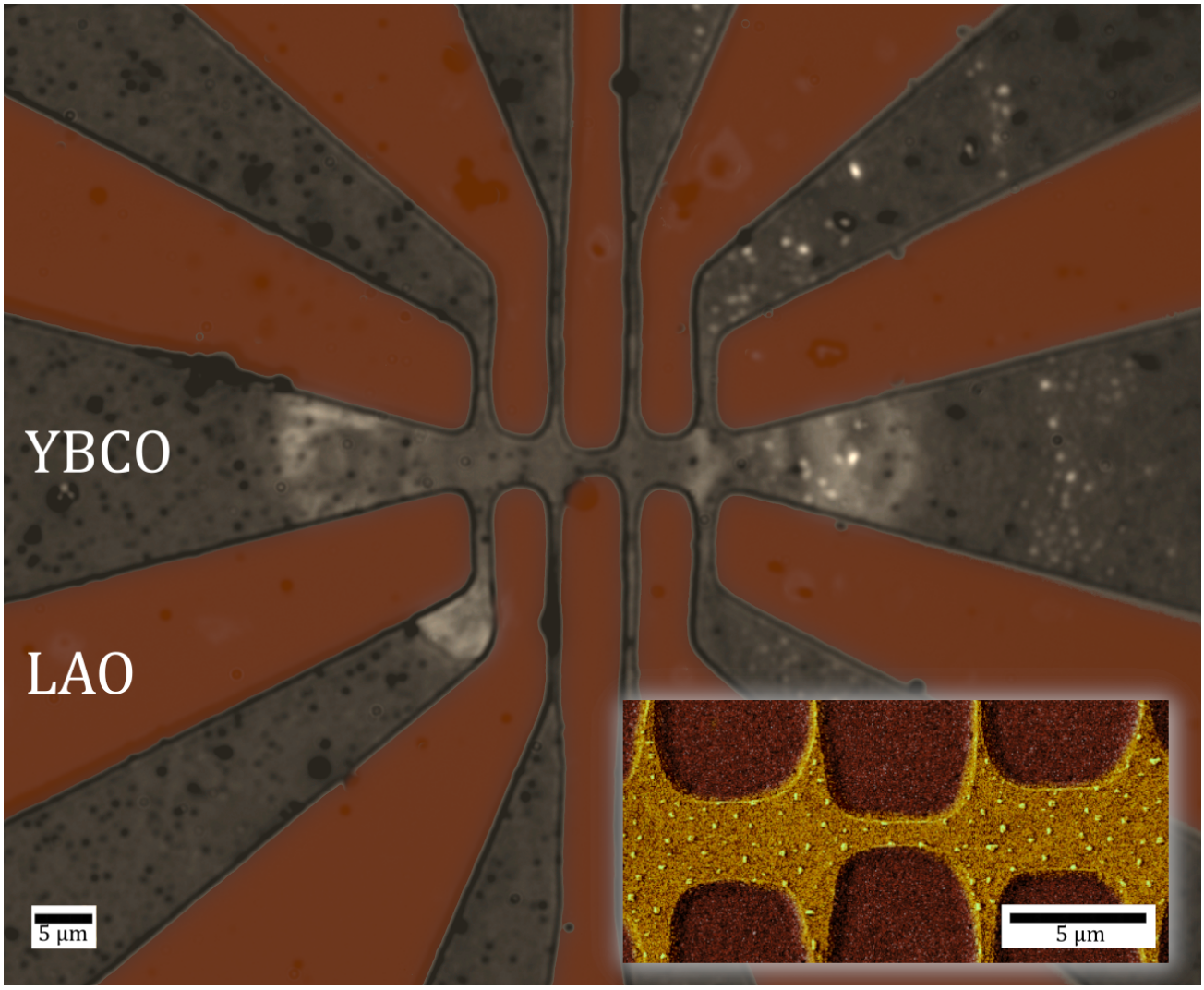

Figure 1: Optical microscopy image of the entire device after electromigration. The inset shows a scanning electron microscopy image of the three central bridges.

regime of decreasing resistance with time. A real time evolution of the optical microscopy images is available in the SI for a similar device. In order to understand this behavior, it is necessary to invoke the displacement of oxygen vacancies from right to left and a simultaneous counterflow of oxygen ion. Within this scenario, the increase of the resistance with time corresponds to the propagation of the front consisting of an area of depleted oxygen in between the corresponding voltage probes. Eventually, the trail of that front is reoxygenated and leads to a decrease of resistance. An optical image of the oxygen-poor front (brighter color) obtained few seconds after applying 8 mA is shown in the inset of the middle panel. The origin of the observed increase of reflectance when the oxygen content decreases has been investigated by Kircher et al.[15] by measuring the dependence of the dielectric tensor on the oxygen stoichiometry. Additional experiment with lower alternative DC polarity are available in the SI.
Figure 3 shows the results obtained from numerical simulations for similar continuous current stress. The initial reduced concentration (see Methods) $x_0 = 0.76$ has been chosen so as to approach the experimentally determined $R(T)$ of the bridges. In addition, a disorder in oxygen distribution of $\delta x_0 =$ 5 % with respect to the mean value x_0, has been assumed. In ref.[13] it has been shown that after electromigration part of the bridge becomes deoxygenated down to a certain minimum value x_{min} whereas other zones are oxygenated up to an upper value x_{max}. This can be understood as a consequence of a concentration-dependent activation energy $E_a(x)$. In the present case, we have taken $x_{min} = 0.5$ and $x_{max} = 0.95$.

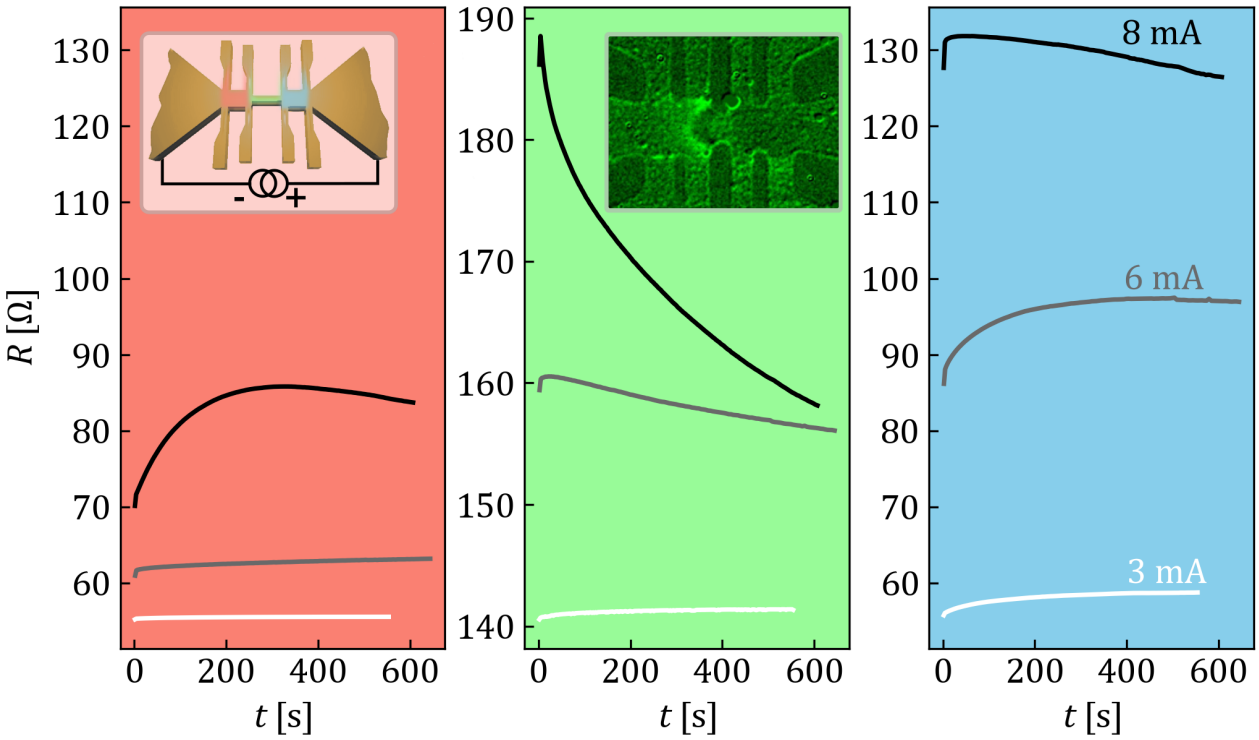

Figure 2: Experimental evolution of the resistance as a function of time under continuous electrical stress for the left, central, and right bridges. The inset in the left panel shows the polarity of the current source and the color code associated to each bridge. An optical microscopy image of the electromigrated YBCO device is shown as inset of the central panel. Higher reflectivity (brighter zone) reveals the region with oxygen deficiency. Measurements performed at room temperature and in ambient conditions.

For 3 and 6 mA the simulations show an initial resistance increase followed by a very stable state. The fact that this stability plateau is reached in much shorter time-scale than in the experimental measurements, suggests that in the experiments the entire substrate is heated by the current whereas in the simulations we assume that the bottom of the substrate is at a fix temperature. For 8 mA DC current, the simulations reproduce the observed experimentally trend and confirm that the initial increase of resistance produces a propagating front of depleted oxygen distribution, whereas the resistance decrease is caused by an oxygenation process. The inset in the middle panel of Figure 3 shows a mapping of the oxygen distribution obtained under the same conditions as the snapshot shown in the inset of Figure 2. The similarities are apparent: a bright arc-shaped front corresponding to the oxygen depleted zone emerges from the central bridge, with a counter-propagating red color front indicating excess oxygen. Note that the optical images clearly reveal the oxygen depleted zone, but are less sensitive to the zone where oxygen content has increased.

2.1.2 AC current stress

The above described approach consisting of a constant bias current suffers from uncontrolled modifications to the sample and eventually by thermal runaway causing permanent damage to the bridges. In addition, it is inconvenient for imaging since the oxygen diffusion proceeds during the acquisition time of the CCD camera. To avoid these drawbacks, we resort to current pulsed measurements following the protocol shown in Figure 4(a). Two consecutive probe current pulses of constant amplitude (I_{probe} = 10 μA) and opposite polarity of 10 s duration are averaged to obtain the total resistance of the sample, i.e. in between the external voltage contacts as shown in Figure 4(b). The probe pulses are followed, after 5 s, by 10 s pulsed current of variable amplitude I_{PLS}. After each pulse, the current is cut off for 5

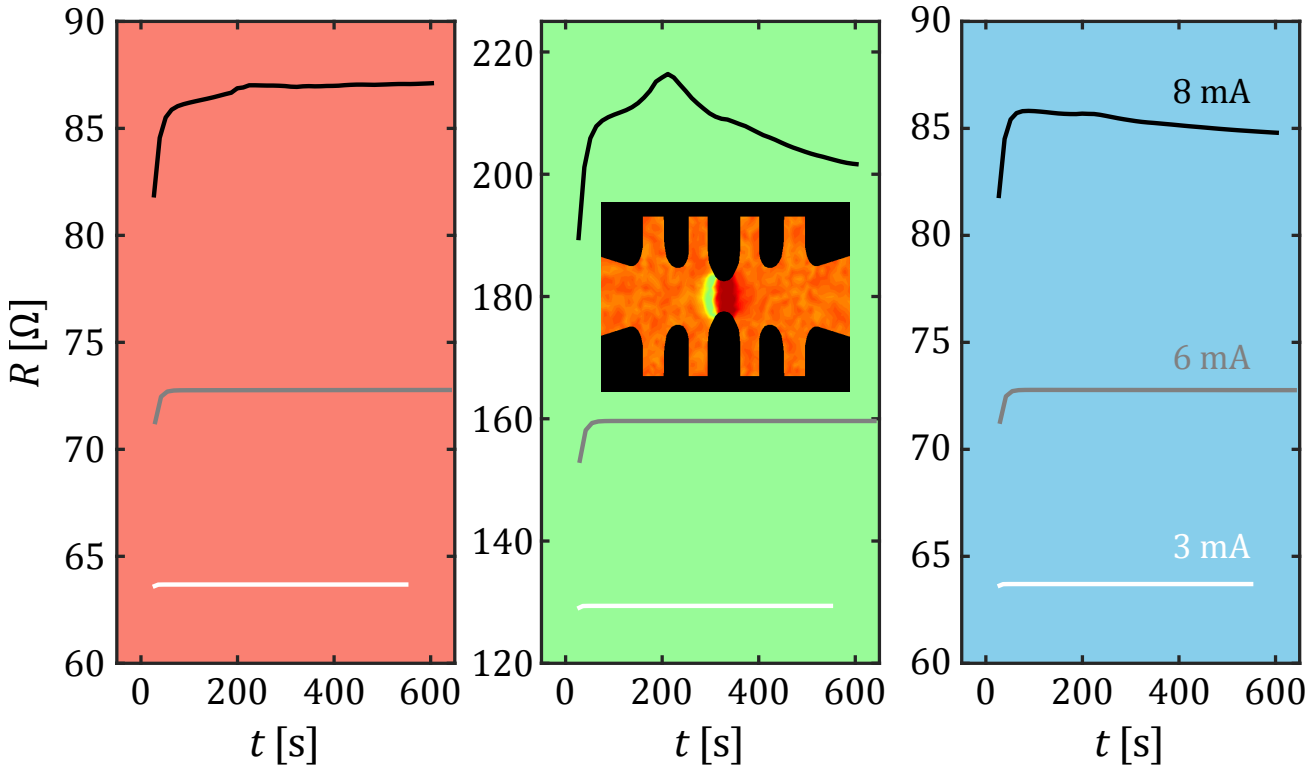

Figure 3: Evolution of the resistance as a function of time under continuous electrical stress for the left, central, and right bridges as obtained by finite-element modeling with $E_a = 0.7$ eV, $x_0 = 0.76$, $x_{min} = 0.5$, $x_{max} = 0.95$ and $\delta x_0 = 5$ %. Inset in the middle panel shows a mapping of the oxygen distribution (yellow / green color indicates the oxygen depleted zone and red color the oxygen rich zone).

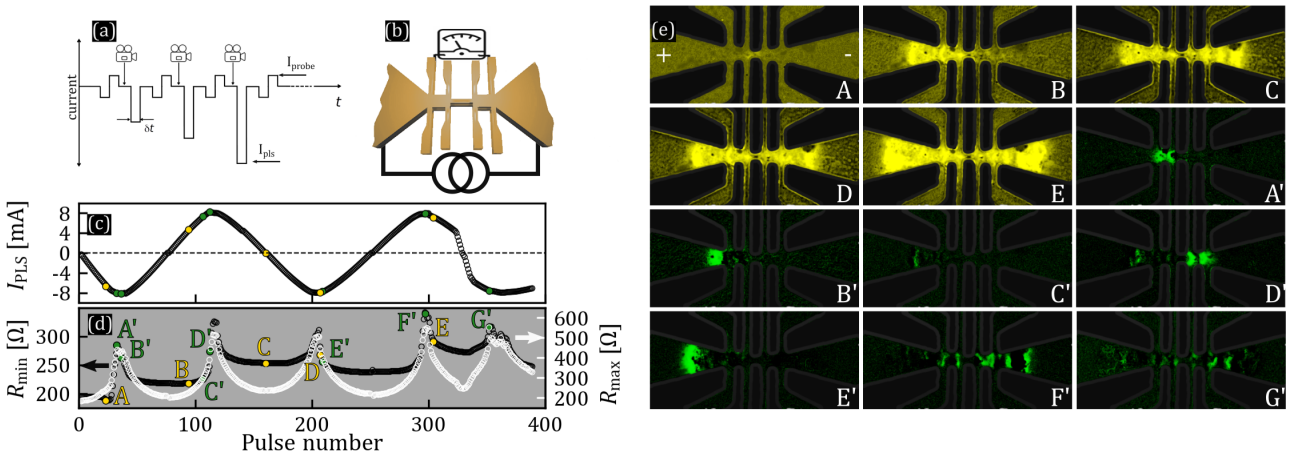

Figure 4: (a) A bipolar I_{probe} pulsed current is used to monitor the sample resistance whereas a $I_{PLS} \gg I_{probe}$ of variable amplitude triggers the electromigration process. Optical microscopy images are acquired after each probe pulse. (b) The total sample resistance picked up by the external electrodes is monitored before and during the I_{PLS} excitation. The panel (c) shows the evolution of I_{PLS} and the panel (d) the resulting evolution of sample resistance before (black points, left axis) and during (white points, right axis) the application of I_{PLS}. Representative optical microscopy images at different stages of the electromigration process are shown in (e). Images labeled A-E acquired at the corresponding yellow points in panel (c), provide direct optical contrast of the affected areas. Images labeled A'-G' acquired at the corresponding green points in panel (c), provide differential optical contrast of the affected areas.

s, much longer than the characteristic time of thermal relaxation ($\sim$ μs),[16;17] to allow the sample to cool down to bath temperature. The panel (c) shows the oscillating I_{PLS} with a maximum amplitude of 8 mA. In the panel (d) the evolution of the total resistance of the device resulting from the oscillating

train of pulses is shown. Black circles correspond to the total resistance after the current pulse has been applied, i.e. remanent resistance (left axis) whereas the white circles correspond to the total resistance during the current pulse (right axis). The latter exhibits a parabolic shape resulting from the Joule heating and the temperature dependent resistance of the device whereas the former remains unaffected by the Joule heating and represents a more convenient tool for unveiling the irreversible changes induced by the electromigration process.

For current pulses up to $I_{PLS} \sim 6$ mA, the remanent resistance of the device remains invariable, meaning that the sample has not undergone any modification. For 6 mA $< I_{PLS} <$ 7 mA, a slight decrease of the sample resistance is observed. As demonstrated by Moeckly *et al.*[10] this effect cannot be solely ascribed to a thermal annealing process resulting from Joule heating but in addition, a current stimulated redistribution of chain oxygen vacancies needs to be invoked. This initial healing of the sample is followed by a rapid increase of the resistance associated to long-range oxygen migration. Interestingly, when I_{PLS} starts to decrease, the sample undergoes a healing process, even though the current flow does not change polarity. The maximum of resistance recovery is obtained for $I_{PLS} \sim 0$. Note that the recovery is incomplete, meaning that the sample experiences irreversible deterioration.[18] Inverting the current polarity does not provide much further healing but rather leads to another increase of resistance followed by a plateau. As current amplitude alternates, a similar sequence of resistance peak-plateau stages develops with the general trend towards an overall progressive deterioration of the device. This observation suggests that low frequency AC-excitations may represent an effective way to increase the resistance of the transport bridge in a controlled fashion.[14;19]

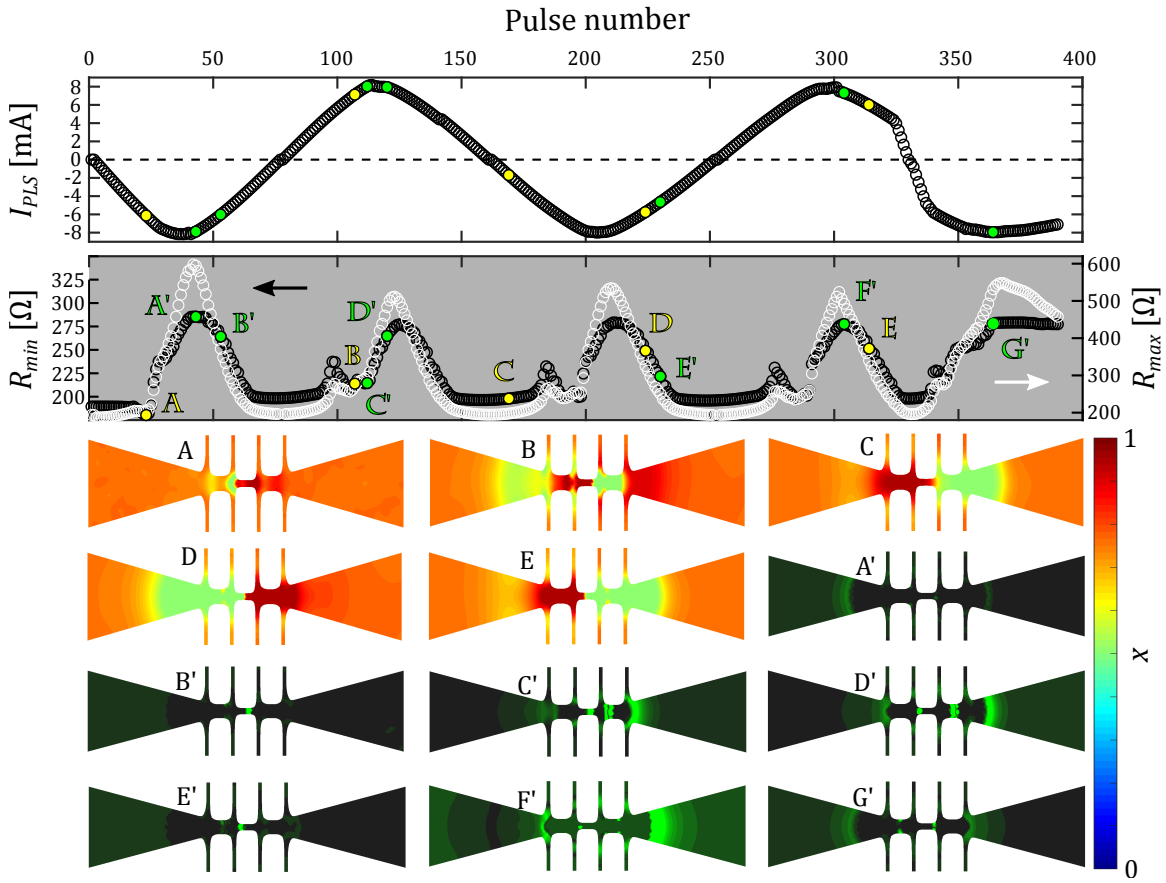

Figure 5: Finite element modeling of the resistance and oxygen cartography evolution as a function of an oscillating current pulse I_{PLS}. For the sake of convenience, the I_{PLS} as a function of pulse number already shown in Figure 4(c) is replotted here. The simulated R_{max}, R_{min}, oxygen concentration, and differential concentration mappings are to be directly compared with the experimental data presented in Figure 4.

Let us now analyze the induced inhomogeneous oxygen distribution as revealed by in situ optical microscopy. A selected set of images is presented in Figure 4(e) corresponding to different stages during the

electromigration cycle process. A complete animation is available in the SI. For images A to E taken at the yellow points indicated in panel (c), the image corresponding to the initial pristine state has been subtracted in order to improve the contrast. Point A corresponds to the onset of electromigration which becomes visible at the central bridge, where the current density and the local temperature are the largest. Point B, taken at the plateau of resistance, shows the extent of the oxygen depletion zone (brighter region) obtained after reaching the maximum current amplitude. At this point the resistance of the device has decreased as a consequence of a partial replenishing of oxygen atoms in between the outer voltage probes. Point C is obtained after inverting the current direction and together with the image corresponding to point B, demonstrates the directional character of the eletromigration process, with oxygen vacancies moving with hole carriers. In D and E, the affected area has further expanded outside the external voltage probes, and therefore it is not captured by the electrical measurements.
When the current direction is inverted, the change of oxygen content in already affected areas becomes nearly imperceptible in the bright microscopy images. A convenient way to unveil these changes is to subtract consecutive images as shown in frames A' - G' of Figure (e). The point A' is taken at the first maximum of resistance and shows that modification of the oxygen content takes place mainly on the left bridge. Point B' corresponds to the maximum current amplitude and shows that oxygen vacancies are mainly affecting the cathode side (-) which lies outside the outer voltage probes. The fact that the resistance has decreases indicates that in turn, oxygen ions are replenishing the previously oxygen-depleted zone in between the voltage probes. When inverting the current direction (C' and D') the oxygen content changes are rather minor in the already affected areas and more prominent in the unaffected right bridge zone. Images E',F', and G' show that further oxygen displacement in these previously modified regions does not happen locally as it would be the case for a single propagating front but in waves extending throughout the device. The reason for this effect lies on the multiterminal geometry of the sample which induces an inhomogeneous current distribution and hot spots of current crowding (see SI).

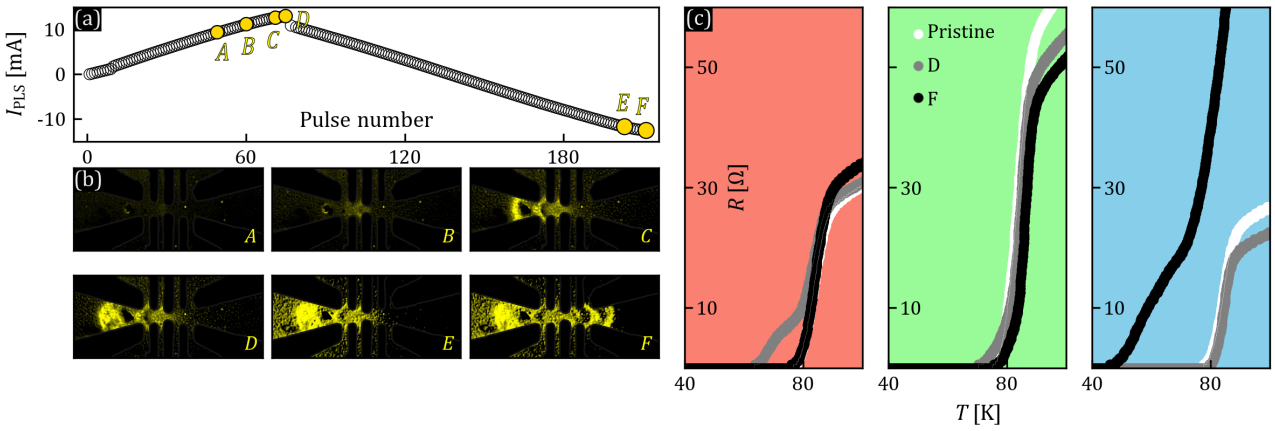

Figure 6: (a) Amplitude of the current pulse I_{PLS} as a function of pulse number. (b) Optical microscopy images corresponding to the points labeled in panel (a). The brighter yellowish zones correspond to oxygen depleted areas. (c) Resistance vs temperature showing the superconducting transition at the left (salmon panel), central (green panel), and right (blue panel) bridges, respectively. The response of the pristine sample is shown with white points, after reaching maximum current amplitude is shown with gray data points, and after reaching maximum current of opposite polarity is shown with black points.

The results of finite element modeling of oxygen diffusion, for the case of pulsed electromigration are shown in Figure 5. The same train of current pulses and overall measurement protocol as in the experiment presented in Figure 4 are reproduced in the simulation. The parameters used for these simulations ($E_a = 0.4$ eV, $x_0 = 0.76$, $\delta x_0 = 5\%$, $x_{min} = 0.5$, $x_{max} = 0.95$) have been chosen so as to approach the experimentally determined initial $R(T)$ of the device and the extent of affected area. Panels A-E show the oxygen concentration mappings and panels A'-G' indicate differential changes in the oxygen concentration at selected points during the electromigration process. The resistance oscillations before

(black points) and during (white points) the pulse, qualitatively capture the features observed experimentally. The permanent changes in sample resistance start to happen for a current of 6 mA. The decrease of sample resistance at point A, results from the oxygenation of an initially less than optimally doped sample ($x_0 = 0.76$). Note that this reoxygenation takes place mainly at the central bridge where the current density is higher and which contributes the most to the total resistance (i.e. in the pristine state, ∼50 % of the resistance measured at the outer probes comes from the central bridge). This local minimum is followed by a rapid increase of resistance as the oxygen depleted zone propagates to the left side. At the maximum of resistance, the local temperature reaches 671 K. Consistent with the experimental observation, a healing process evidenced by a decrease of resistance occurs when the pulsed current amplitude decreases. We attribute this effect to the thermally activated relaxation process. Indeed, even though the applied current is smaller than that needed to induce electromigration, Joule heating rises substantially the local temperature and induces a relaxation process driven by the pronounced gradient of oxygen concentration that will partially reoxygenate the central bridge (see equation (1)). Below certain current threshold no further changes are observed (oxygen diffusion is halted) and a resistance plateau develops. This resistance plateau exceeds the initial resistance of the sample which, implies irreversibility in the electromigration process. Note that the modeling produces a lower irreversibility than the one observed experimentally. This is also visible in the oxygen concentration mapping. Indeed, when comparing points B and C, one can remark that at point C the previously deoxygenated region on the left side of the device has been replenished and reoxygenated. To explain this discrepancy between theory and experiment, one can invoke a concentration dependent activation energy (see discussion bellow for more details) or simply oxygen loss to the environment due to the high temperatures attained during the electromigration process. The modeling also shows local satellite maxima just before reaching the maximum current amplitude. The origin of this satellite peak is that the high temperature and electric field at the central junction generate a better oxygen mobility and consequently a higher oxygen flux than the neighboring junctions. In the case of a current moving oxygen to the right, this creates an oxygen defect on the left side of the central bridge that cannot be directly supplied with oxygen coming from the left. This temporarily produces an oxygen defect in the central bridge and thus gives rise to an increase in resistance. Interestingly the differential images A'-G' confirm that changes in the concentration during the current reversal take place simultaneously throughout the entire structure instead of in a single propagating front.The complete simulation showing maps of oxygen content, temperature, current density and electrical field of the results discussed in this section is available in the SI.

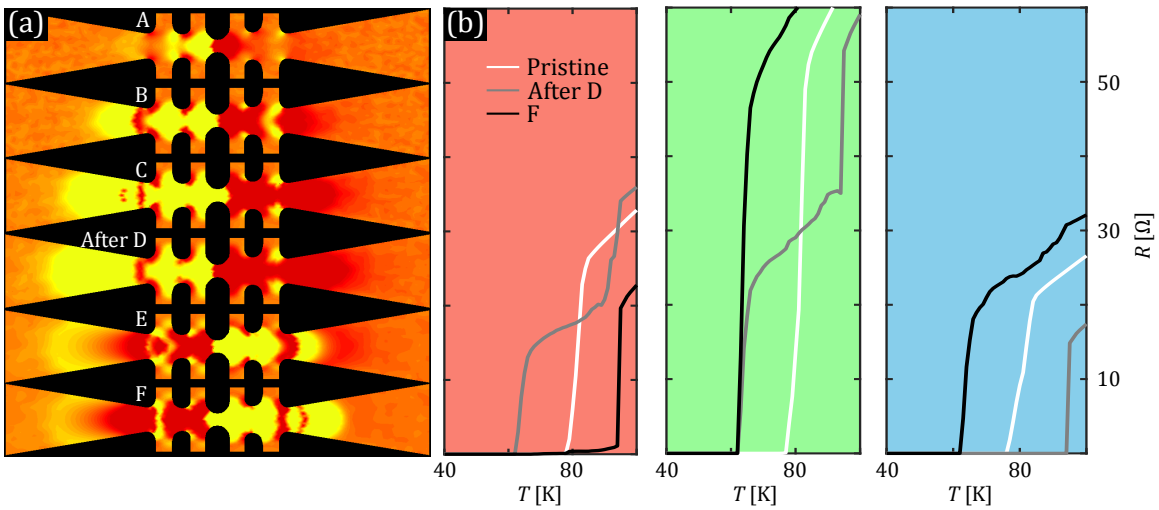

Figure 7: Panel (a) shows the simulated oxygen maps for the same points A → F as shown in Figure 6(a) except for the fourth point (formerly D) which is now taken after D. The red and yellow colors correspond to oxygen-rich and oxygen-poor areas respectively. (b) $R(T)$ curves for the left, center and right bridges. The color convention used is the same as in Figure 6(c). The parameters for these simulations are $E_a = 0.7$ eV, $x_0 = 0.76$, $x_{min} = 0.5$, $x_{max} = 0.9$ and $\delta x_0 = 5$ %.

Thus far we have investigated the global response of the entire device as the train of pulses oscillate in

amplitude driving oxygen vacancies back and forth. We can obtain further insights by analyzing the local modifications operating in each individual bridge. Figure 6 shows the $R(T)$ response at the left (salmon panel), central (green panel) and right (blue panel) bridges for the initial (pristine) state (white dots), after reaching the maximum applied current (point D, gray dots) and after reversing the polarity of the current up its maximum value (point F, black dots). Some representative optical microscopy snapshots for the points indicated as A,B,...,F are shown. As evidenced by the snapshot D, the maximum applied current (from right to left) gives rise to a substantial diffusion of oxygen vacancies, way beyond the outer voltage contact. After this electromigration run, we observe that the right bridge exhibits a reduction of the normal state resistance and a slight increase of the superconducting critical temperature. The central bridge also exhibits a decrease of the normal resistance which is concomitant with a slight increase of T_c, whereas the left bridge shows increased normal state resistance and a double step transition. By inverting the applied current polarity, thus replenishing of oxygen at the left bridge and inducing oxygen vacancy displacement towards the right bridge, a healing of the resistance of the left bridge and a clear deterioration of the conducting properties at the right bridge are observed. This is consistent with the optical image shown in panel F.
As shown in Figure 7, the numerical modeling, assuming similar conditions as in the experiment, is able to qualitatively capture most of the features and trends observed experimentally. Note that the simulations predict that both central and left bridges should be severely affected by the electromigration process, exhibiting a double-step transition. This is in agreement with measurements obtained by controlled electromigration as reported in Figure3b and FigureS2 of ref.[13]. Nevertheless, some discrepancies between the experiment and the model can be pointed out. Namely, (i) the amplitude of the resistance and critical temperature changes differ and (ii) the observed healing effect upon current polarity reversal is less pronounced than predicted numerically. As we have stressed above, these discrepancies might arise from important ingredients that are not taken into account in the present model, such as the effect of oxygen chain ordering, oxygen content-dependent activation energy and loss of oxygen into the environment.

2.1.3 Effect of modeling parameters

Now that we have validated the proposed numerical model through direct comparison with experiments, it is interesting to further scrutinize the influence of the different parameters involved in the model on the electric response of the device and the spatial extent of oxygen diffusion. To that end, in Figure 8 we monitor the resistance at remanence (i.e. after each current pulse) R_{min} and during the pulse R_{max} as a function of a pulsed current amplitude that increases linearly from zero and reaching a maximum value of 8 mA at pulse 40 and then decreasing linearly down to zero at pulse number 80. Panels (a) and (b) along with snapshots A-E show the influence of the activation energy E_a. For $E_a \geq 0.4$ eV the electromigration first induces a small resistance drop before leading to a resistance increase, consistent with the experimental findings. As expected the larger E_a the higher the current density needed to trigger electromigration. In addition, as E_a decreases the maximum resistance achieved increases and consequently so does the Joule heating. Therefore, for lower E_a the attained highest temperature along the bridge increases (panel (b)) and the oxygen diffusion further expands into the leads (snapshots A-E).
Figure 8 (c) and (d) show the resistance change when x_{min} is varied while the rest of the parameters remain constant. As a reminder, limiting the amplitude of the reduced concentration x is a zeroth-order approximation to account for a concentration-dependent activation energy. Allowing to access smaller values of oxygen concentration leads to more pronounced modifications of the resistance and higher temperatures (panel (d)) although not major modifications are observed in the spatial extend of the diffusion (snapshots F-G). Interestingly, we have found that modifications on the parameters maximum oxygen concentration x_{max}, the initial oxygen concentration x_0, and the amplitude variation around the mean value δx_0 have minor impact on the final state (see SI). In brief, the activation energy and the lowest achievable oxygen concentration are the key parameters ruling the extent of the oxygen diffusion. This finding suggests that the activation energy should depend on the actual oxygen concentration.

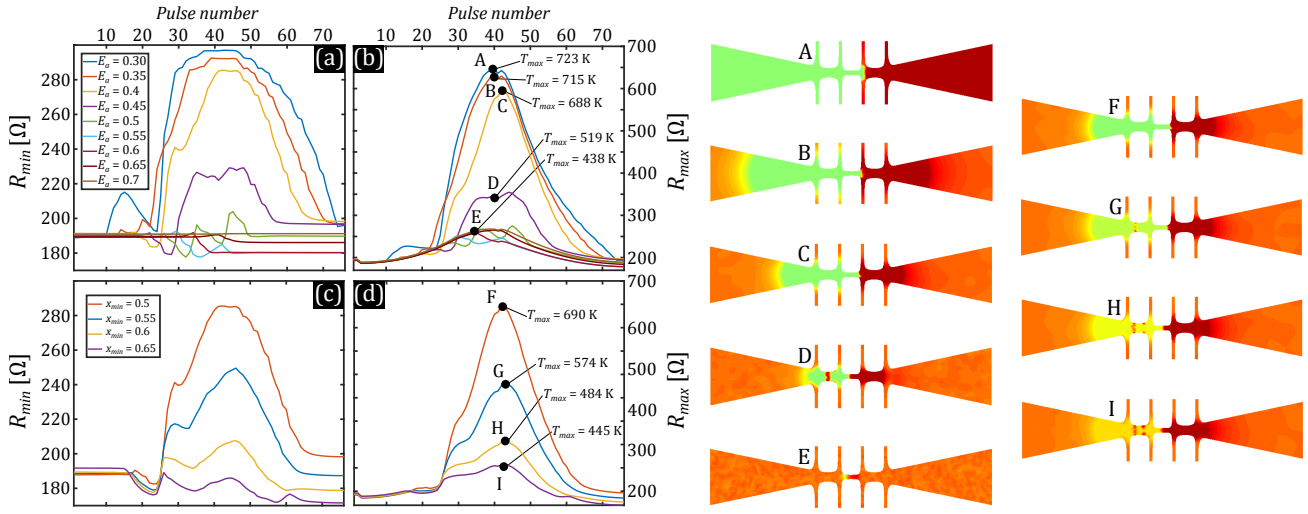

Figure 8: The evolution of R_{min} and R_{max} for different activation energies are given in panels (a) and (b) respectively (E_a is given in eV). The other parameters remain unchanged: $x_0 = 0.76$, $x_{min} = 0.5$, $x_{max} = 0.95$ and $\delta x_0 = 5$ %. Panels (c) and (d) show R_{min} and R_{max} for several x_{min} and constant activation energy $E_a = 0.4$ eV. The snapshots on the right show the oxygen distribution for the corresponding points A - I indicated in panels (b) and (d). The maximum attained temperatures are shown in panels (b) and (d).

2.1.4 Oxygen concentration dependent activation energy

The extended mobility of oxygen in YBCO is, as mentioned above, greatly due to the presence of vacant sites in close proximity to the moving atoms, allowing for a less energetic diffusion mechanism by interstitials in comparison to substitution mechanisms.[20;21] This can aid in understanding why many reports, including those mentioned in the introduction, show a smaller diffusivity of O with lesser oxygen content. A good indicator of the oxygen ordering in many complex oxides are the elastic properties, accessible via acoustic relaxation measurements as shown in the work of Cannelli *et al.*.[22] The elastic energy loss of YBCO with variable δ is shown to be distinct and to include separate structural phase transitions, that occur at varying temperatures. The same authors show that, as a function of oxygen content, the intensity of the three identified structural phase transition peaks shift,[23] with two of them, appearing at 400-600 K being characteristic of orthogonal YBCO and tetragonal YBCO having its characteristic peak at significantly lower temperatures. The observed elastic energy loss is due to oxygen diffusion and ordering in the orthorhombic lattice, and the activation energy of this process ($\sim$ 1.1 eV) is higher than expected as one must take into account the restructuring of the whole orthorhombic oxygen chains to accommodate further oxygen into the lattice. This is in agreement with the idea that twinning in optimally-doped YBCO is a way to relieve strain from the highly non-stoichiometric structure of the material. Seeing the increase in E_a for both lower (as diffusion by substitution is more energetically demanding) and higher oxygen levels (due to orthorhombic oxygen chain restructuring), one could make an argument for a parabolic shape of the oxygen diffusivity in the material, as has been seen for similar perovskite oxides by Yoo *et al.*[24] Looking for a good first approximation to model the experimental data, we will now assume that our mobile oxygen has a peak diffusivity somewhere in the non-stoichiometric region. Therefore, we propose in this section to investigate the effect of a parabolic $E_a(x)$ by imposing that the average value over the allowed range of x is constant and equal to 0.4 eV. The lowest value of the activation energy $E_{a,min}$ allows to label the different profiles.
Figure 9(a) shows the evolution of R_{min} versus time for the profiles of $E_a(x)$ given in Figure 9(b). We observe that the final resistance increases as $E_{a,min}$ decreases. This result can be interpreted as follows: in the initial state the homogeneity of the oxygen concentration also implies homogeneity of the activation energy (close to the minimum of the parabola). The central bridge, where the electric field and temperature peak, will quickly generate an asymmetric distribution of oxygen and consequently increase the activation energy in the left and right bridges which will have a reduced mobility when the current

changes polarity. This difference in mobility implies different oxygen concentrations and therefore different resistances between the final and initial states. We therefore define the parameter $\Delta R = R_{final} - R_{init}$ (see Figure 9(a)) as an indicator of irreversibility. The evolution of this parameter as a function of $E_{a,min}$ shown in the inset of Figure 9(b) indicates that an inhomogeneous activation energy accentuates the irreversibility for the oxygen transport. This finding suggests that in order to explain the observed irreversible response of the electromigration process a concentration-dependent activation energy should be invoked. Nonetheless, other effects such as oxygen loss could also play an important role.

3 Conclusion

To summarize, we have performed continuous DC and pulsed electromigration on YBCO while simultaneously recording the electrical signal in a multiterminal bridge and monitoring the oxygen displacement by optical reflectometry . These results are compared to finite element modeling for which current-induced oxygen diffusion is coupled to heat transport, including a temperature and concentration dependent resistivity. The simulations are able to qualitatively and to certain extent quantitatively capture the general trend observed in the experiments (electrical response and oxygen concentration mapping) and allow to estimate the local temperature during the electromigration process and the activation energy associated to the diffusion process. In addition, the model permits us to explore the influence of different parameters such as initial oxygen concentration, oxygen disorder, and activation energy, which would require a colossal effort to address experimentally. These findings might shed light on the recent investigation of DC and AC electromigration in YBCO[14;19] and could be extended to explore the memristive properties of this material[25] or the electrical doping of $Bi_2Sr_2CaCu_2O_{8-\delta}$.[26] The close correlation between experiments and theory may encourage further research to explore the predictive power of the modeling to analyze the retention time and endurance of memristive devices based on oxygen motion and the effect of degassing caused by oxygen out-diffusion. Even though the proposed modeling substantially outperform previous attempts,[13] there are nevertheless further refinements that could be considered at expense of preventing accessible interpretation, such as 3D simulation structure, thermomigration, and a source term in eq. 1 accounting for oxygen loss.

4 Methods

4.1 Experimental details

Epitaxial 50 and 100 nm thick $YBa_2Cu_3O_{7-\delta}$ films were grown with the c-axis aligned perpendicular to the film plane, by pulsed laser deposition on $LaAlO_3$ single crystal substrates. For ensuring ohmic electrical contacts, 200 nm thick Ag electrodes were sputtered and annealed by heating in an oxygen-rich environment. The films were patterned via photolithography and dry ion-beam etching into multiterminal triple constrictions.
The optical microscopy images were obtained under atmospheric conditions with a 50× magnification objective (NA = 0.5) followed by a 2× magnification lens and collected in bright field mode with a continuous green illumination filtered from a Hg lamp. The optical microscopy imaging is performed simultaneously with the electrotransport in order to be able to make a reliable comparison of the electromigration effects.

4.2 Finite elements modeling

The model considers the YBCO sample as a continuous material whose state can vary locally between tetragonal or orthorhombic configurations corresponding to oxygen concentration c between $c_{min} = 3.41 \times 10^{28}$ and $c_{max} = 4.01 \times 10^{28}\,\mathrm{ions\,m^{-3}}$, respectively.[27] We further assume that only the oxygen in excess to the tetragonal state can contribute to the oxygen diffusion[28] and define the adimensional variable $x = (c - c_{min})/(c_{max} - c_{min})$ to distinguish between insulating ($x = 0$) and superconducting ($x = 1$)

states. It is assumed that the temporal evolution of x is governed by equation (1). The first term on the right-hand side represents a conventional diffusion process due to an inhomogeneous distribution of oxygen while the second term comes from the combined effect of electron wind and electric field as a consequence of an applied voltage V :

$$\frac{\partial x}{\partial t} = \nabla(\mathbf{D}.\nabla x + z\mathbf{u}Fx\nabla V) \tag{1}$$

Here $\mathbf{D}$ is the temperature dependent isotropic diffusion tensor with $D = D_0 \exp(-E_a/k_B T)$ and $D_0 = 1.4 \times 10^{-8}\,\mathrm{m^2\,s^{-1}}$,[4] E_a is the activation energy in eV, k_B is the Boltzmann constant, z the charge number of oxygen ions, $\mathbf{u}$ the Nernst-Einstein ration ($\mathbf{u} = \mathbf{D}/RT$) and F is the Faraday number. In addition, the heat equation (2):

$$\rho_m C \frac{\partial T}{\partial t} = \kappa \nabla^2 T + \rho(x,T)\mathbf{j}^2 \tag{2}$$

is solved in order to obtain the spatial distribution of temperature T, where ρ_m is the density in kg m^{-3}, C the specific heat capacity in J kg^{-1} K^{-1}, T the temperature in K, κ the thermal conductivity in W K^{-1} m^{-1}). The second term on the right-hand side of equation (2) represents the Joule heating and involves the resistivity of the material which depends on both the concentration and local temperature. The functionality $\rho(x,T)$ imposed in the model is taken from experimental values reported in ref.[29] (see Figure 10(a)). For $T > 300\,\mathrm{K}$, we assume a linear dependent resistivity $\rho(x,T) = [1+\alpha(T-T_{ref})]\rho(x,T_{ref})$ with $\alpha = 5 \times 10^{-3}\,\mathrm{K^{-1}}$ determined by $R(T)$ measurements and $T_{ref} = 300\,\mathrm{K}$.
Finally, the Poisson equation is solved to obtain the electric potential distribution in the sample:

$$\nabla^2 V = 0 \tag{3}$$

Note that the right-hand term of equation (3) is set to zero in order to guarantee charge neutrality throughout the device. The electric field $\mathbf{E} = -\nabla V$ is related to the current density $\mathbf{J}$ by Ohm's constitutive equation $\mathbf{J} = \mathbf{E}/\rho(x,T)$ and does not take into account the ionic current whose contribution is negligible.[28] The solution of the system of equations (1),(2) and (3) with proper boundary conditions is obtained for the exact geometry of the real sample, using the finite element software COMSOL.[30] A top view of the layout and the mesh used for FEM simulations is shown in Figure 10(b). Due to the small thickness/width aspect ratio, a 2D version of the equations (1), (2) and (3) is solved for the YBCO layer while only equation (2) is solved for the substrate. The values of the thermal coefficients are listed in the Table 1. Slightly different thermal coefficient as reported in refs.[31;32] lead to similar results.

	ρ_m [kg m^{-3}]	C [J kg^{-1} K^{-1}]	κ [W K^{-1} m^{-1}]
LAO	6520[33]	450[33]	11.7[33]
YBCO	6300[34;35]	520[36;37]	10[37]

Table 1: Thermal coefficients used as input parameters in COMSOL simulations.

Having a system of coupled equations combined with logarithmic behavior of resistivity with concentration makes simultaneous resolution particularly demanding. In order to speed up the numerical calculations, an iterative time process with two steps per iteration is used. First, the temperature and potential profiles are evaluated at iteration i assuming x to be constant as determined in the previous iteration $i-1$. During this step, the temperature dependence of the resistivity is assumed to be the temperature profile from previous iteration. Second, the new spatial distribution of the concentration x is calculated assuming T and V constant. The values T, V and x at the first iteration are given by the initial conditions of the problem. It is worth noting that equations 1 and 3 have been solved in ref.[13] but omitting the heat equation 2, the fact that the resistivity is temperature and concentration dependent, and also ignoring the exact geometry of the sample.

Supporting Information
Supporting Information is available from the Wiley Online Library or from the author.

Acknowledgements
We thank Xavier Granados for useful discussions. This work was supported by the Fonds de la Recherche Scientifique - FNRS under the grants CDR J.0151.19, EQP U.N027.18 and PDR T.0204.21 and the COST action NanoCoHybri (CA 16218). S. Marinković acknowledges support from FRS-FNRS (Research Fellowship ASP). The authors acknowledge financial support from Spanish Ministry of Economy and Competitiveness through the "Severo Ochoa" Programme for Centers of Excellence in R& D (CEX2019-000917-S) and SuMaTe project (RTI2018-095853-B-C21), cofinanced by the European Regional Development Fund, and from the Catalan Government (2017-SGR- 1519).
S.Collienne and Stefan Marinković contributed equally to this work.

Conflicts of interests
The authors declare no conflicts of interest.

References

[1] B. Keimer, S. A. Kivelson, M. R. Norman, S. Uchida, J. Zaanen, *Nature* **2015**, *518* 179.

[2] M. Ronay, P. Nordlander, *Physica C* **1988**, *153* 834.

[3] K. Tu, N. Yeh, S. Park, C. Tsuei, *Phys. Rev. B* **1989**, *39* 304.

[4] S. J. Rothman, J. L. Routbort, J. E. Baker, *Phys. Rev. B* **1989**, *40* 8852.

[5] B. W. Veal, A. P. Paulikas, Y. Shi, H.and Fang, J. W. Downey, *Phys. Rev. B* **1990**, *42* 6305.

[6] J. Choi, M. Sarikaya, I. A. Aksay, R. Kikuchi, *Phys. Rev. B* **1990**, *42* 4244.

[7] C. Krauns, H. Krebs, *Z. Phys. B* **1993**, *92* 4346.

[8] R. Baetzold, *Phys. Rev. B* **1990**, *42* 56.

[9] S. J. Rothman, J. L. Routbort, U. Welp, J. E. Baker, *Phys. Rev. B* **1991**, *44* 2326.

[10] B. H. Moeckly, D. K. Lathrop, R. A. Buhrman, *Phys. Rev. B* **1993**, *47* 400.

[11] J. LaGraff, D. Payne, *Phys. Rev. B* **1992**, *47* 3380.

[12] T. Wang, J. Cao, X. Gou, *Appl. Surf. Sci.* **2019**, *480* 765.

[13] S. Marinković, A. Fernández-Rodríguez, S. Collienne, S. B. Alvarez, S. Melinte, B. Maiorov, G. Rius, X. Granados, N. Mestres, A. Palau, A. V. Silhanek, *ACS Nano* **2020**, *14* 11765.

[14] E. Trabaldo, A. Kalaboukhov, R. Arpaia, E. Wahlberg, F. Lombardi, T. Bauch, *Phys. Rev. Appl.* **2022**, *17* 024021.

[15] J. Kircher, M. Kelly, S. Rashkeev, M. Alouani, D. Fuchs, M. Cardona, *Phys. Rev. B* **1991**, *44* 217.

[16] C. You, I. Sung, B. Joe, *Appl. Phys. Lett.* **2006**, *89* 222513.

[17] H. Fangohr, D. Chernyshenko, M. Franchin, T. Fischbacher, G. Meier, *Phys. Rev. B* **2011**, *84*, 5.

[18] A. M. Perez-Muñoz, P. Schio, R. Poloni, A. Fernandez-Martinez, A. Rivera-Calzada, J. C. Cezar, E. Salas-Colera, G. R. Castro, J. Kinney, C. Leon, J. Santamaria, J. Garcia-Barriocanal, A. M. Goldman, *Proc. Natl. Acad. Sci.* **2017**, *114* 215.

[19] E. Trabaldo, A. Garibaldi, F. Lombardi, T. Bauch, *Supercond. Sci. and Technol.* **2021**, *34* 104001.

[20] A. Paul, T. Laurila, V. Vuorinen, S. V. Divinski, In *Thermodynamics, Diffusion and the Kirkendall Effect in Solids*, 167–238. Springer International Publishing, **2014**.

[21] V. Sadykov, N. N. Bulgakov, V. Muzykantov, T. Kuznetsova, G. Alikina, A. Lukashevich, Y. V. Potapova, V. Rogov, E. Burgina, V. Zaikovskii, E. Moroz, G. S. Litvak, I. S. Yakovleva, L. Isupova, V. Zyryanov, E. Kemnitz, S. Neophytides, In *Mixed Ionic Electronic Conducting Perovskites for Advanced Energy Systems*, 53–74. Springer Netherlands, **2004**.

[22] G. Cannelli, R. Cantelli, F. Cordero, F. Trequattrini, *Supercond. Sci. Technol.* **1992**, *5* 247.

[23] G. Cannelli, R. Cantelli, F. Trequattrini, F. Cordero, *Jour. of Adv. Sci.* **1995**, *7* 188.

[24] H. Yoo, D. Lee, *Phys. Chem. Chem. Phys.* **2003**, *5* 2212.

[25] A. Schulman, C. Acha, *J. Appl. Phys.* **2013**, *114* 243706.

[26] T. Jacobs, Y. Simsek, Y. Koval, P. Muller, V. Krasnov, *Phys. Rev. Lett.* **2016**, *116* 067001.

[27] J. D. Jorgensen, B. W. Veal, A. P. Paulikas, L. J. Nowicki, G. W. Crabtree, H. Claus, W. K. Kwok, *Phys. Rev. B* **1990**, *41* 1863.

[28] A. Palau, A. Fernandez-Rodriguez, J. C. Gonzalez-Rosillo, X. Granados, M. Coll, B. Bozzo, R. Ortega-Hernandez, J. Suñé, N. Mestres, X. Obradors, T. Puig, *ACS Appl. Mater. Interfaces* **2018**, *10* 30522.

[29] K. Semba, A. Matsuda, *Phys. Rev. Lett.* **2001**, *86* 496.

[30] COMSOL Multiphysics® v. 5.4. COMSOL AB, Stockholm, Sweden.

[31] M. Nahum, S. Verghese, P. L. Richards, K. Char, *Appl.Phys. Lett.* **1991**, *59* 2034.

[32] S. K. Gupta, P. Berdahl, R. E. Russo, G. Briceño, A. Zettl, *Physica C: Supercond.* **1993**, *206* 335.

[33] P. Michael, J. Trefny, B. Yarar, *J. Appl. Phys.* **1992**, *72* 107.

[34] A. Knizhnik, G. E. Shter, G. S. Grader, G. M. Reisner, Y. Eckstein, *Physica C: Supercond.* **2003**, *400* 25.

[35] I. Grekhov, L. Delimova, I. Liniichuk, A. Lyublinsky, I. Veselovsky, A. Titkov, M. Dunaevsky, V. Sakharov, *Physica C: Supercond.* **1999**, *324* 39.

[36] N. E. Phillips, J. P. Emerson, R. A. Fisher, J. E. Gordon, B. F. Woodfield, D. A. Wright, *J. Supercond.* **1994**, *7* 251.

[37] H. Fujishiro, M. Ikebe, T. Naito, K. Noto, S. Kohayashi, S. Yoshizawa, *Jpn. J. Appl. Phys.* **1994**, *33* 4965.

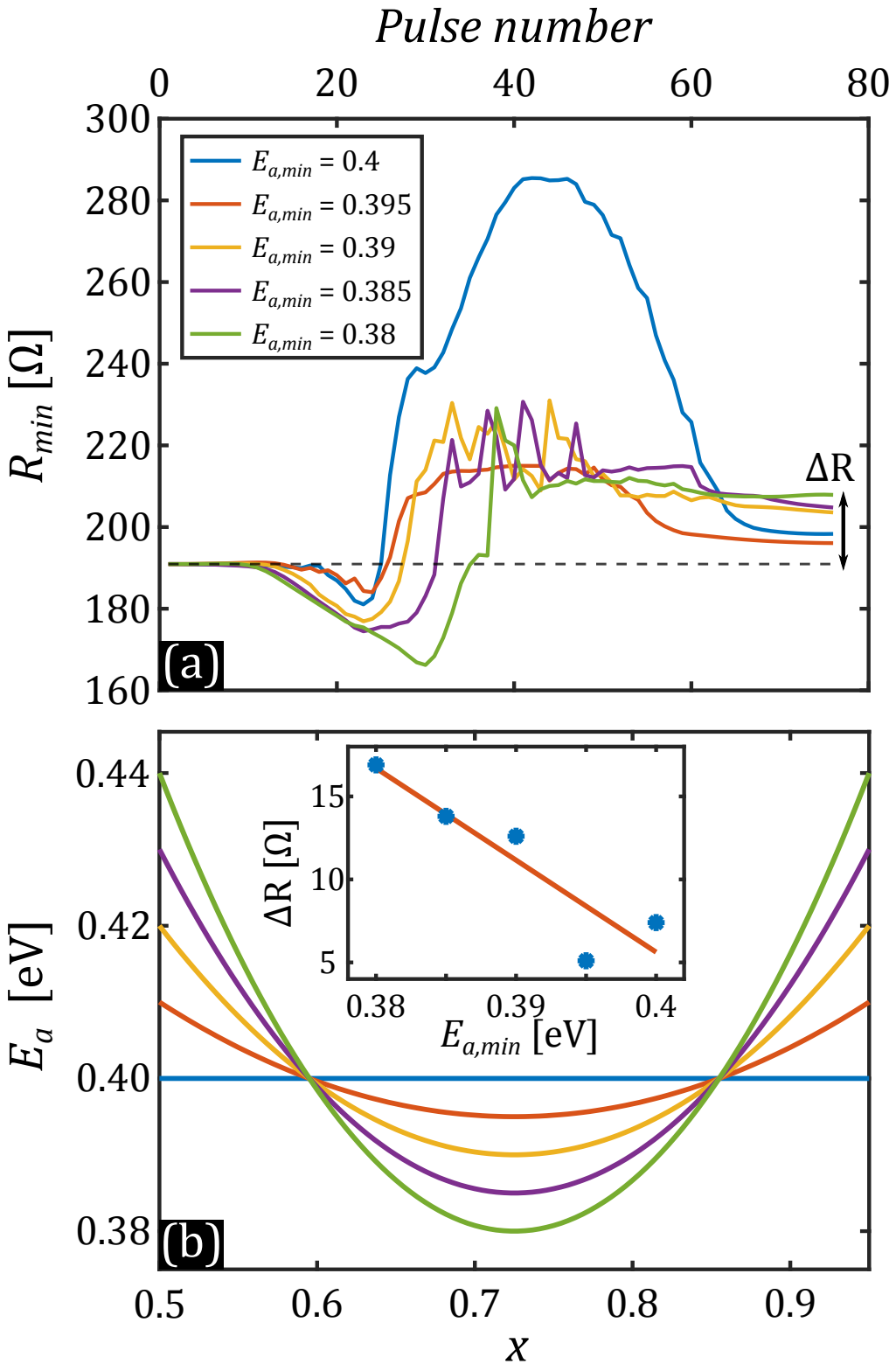

Figure 9: Panel (a) shows the temporal evolution of R_{min} for the different $E_a(x)$ profiles given in panel (b). The observed correlation between the irreversibility parameter $\Delta R = R_{final} - R_{init}$ and the lowest value of the activation energy is given as the inset of panel (b). The others parameters are $x_0 = 0.76$, $x_{min} = 0.5$, $x_{max} = 0.95$ and $\delta x_0 = 5$ %. The value of the applied current corresponds to the first 80 pulses of the Figure 5.

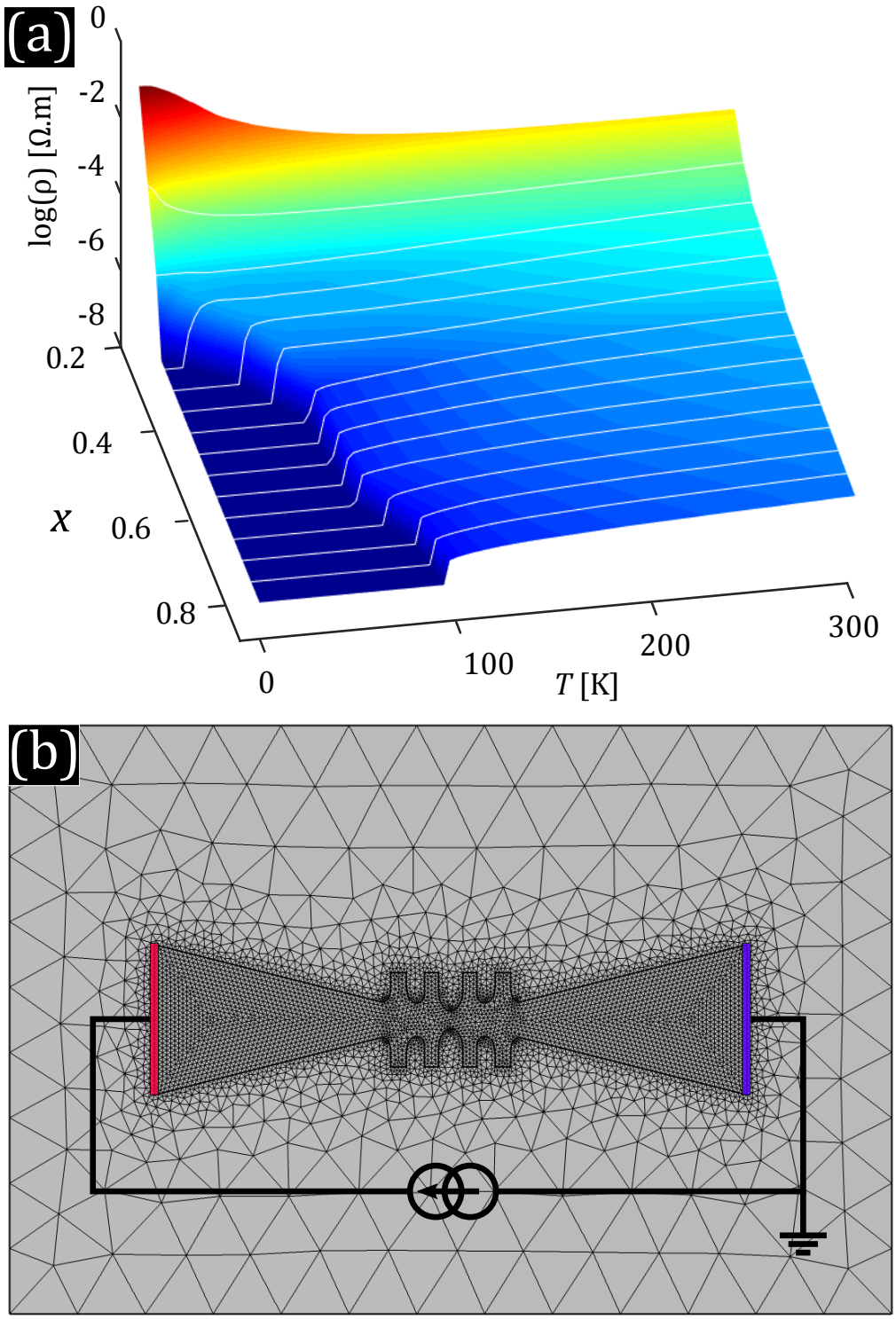

Figure 10: (a) Linear interpolation of $\rho(x, T)$ data extracted from ref.[29]. For values of T above 300 K, a single α value is derived from an $R(T)$ curve for all oxygen concentrations. (b) Top view of the layout and the mesh used for FEM simulations. The positive (red) terminal is simulated as a current source while the negative (blue) terminal is connected to ground. The value of the current injected at each time step of the simulation is dictated by the experimental values.